Electric field gradients at ^{111}In/^{111}Cd probe atoms on A-sites in 211-MAX phases

2011 J. Phys.: Condens. Matter 23 505501

(http://iopscience.iop.org/0953-8984/23/50/505501)

J. Phys.: Condens. Matter **23** (2011) 505501 (19pp) doi:10.1088/0953-8984/23/50/505501

Electric field gradients at ^{111}In/^{111}Cd probe atoms on A-sites in 211-MAX phases

D Jürgens[1], M Uhrmacher[1], H-G Gehrke[1], M Nagl[1], U Vetter[1], C Brüsewitz[1], H Hofsäss[1], J Mestnik-Filho[2] and M W Barsoum[3]

[1] II. Physikalisches Institut, Universität Göttingen, Friedrich-Hund-Platz 1, D-37077 Göttingen, Germany
[2] Instituto de Pesquisas Energéticas e Nucleares, Av. Professor Lineu Prestes 2242, 05508-000 São Paulo, SP, Brazil
[3] Department of Materials Science and Engineering, Drexel University, Philadelphia, PA 19104, USA

E-mail: djuerge@uni-goettingen.de

Received 5 August 2011, in final form 24 October 2011
Published 28 November 2011
Online at stacks.iop.org/JPhysCM/23/505501

Abstract
The method of perturbed angular correlation (PAC) was applied to selected MAX phases with 211 stoichiometry. Radioactive ^{111}In ions were implanted in order to measure the electric field gradients (EFG) in the key compounds Ti_2InC and Zr_2InC to determine the strength and symmetry of the EFG at the In-site. Further PAC studies in the In-free MAX phases Ti_2AlN, Nb_2AlC, Nb_2AsC and Cr_2GeC were performed to confirm that the In probes occupy the A-site as well. The strength of the EFG, with a quadrupole coupling constant ν_Q between 250 and 300 MHz in these phases, is quite similar to the ones found in Ti_2InC with $\nu_Q = 292(1)$ MHz and in Zr_2InC with $\nu_Q = 344(1)$ MHz, respectively. Different annealing behavior was observed whereas in all cases a linear decrease of ν_Q with increasing measuring temperatures was found. The experimental results are also in excellent agreement with those predicted by *ab initio* calculations using the APW+lo method implemented in the WIEN2k code. This study shows in an exceptional manner that $^{111}\text{In} \rightarrow {}^{111}\text{Cd}$ atoms are suitable probes to investigate the local surrounding at the A-site in 211-MAX phases.

(Some figures may appear in colour only in the online journal)

1. Introduction

Hyperfine interaction methods like perturbed γ–γ angular correlation spectroscopy (PAC) have become indispensable in material science to study solids on the atomic scale. Due to their high sensitivity on the local environment of probe nuclei, accurate measurements of electric field gradients (EFG) provide detailed information about structural and electronic properties. Over the last 30 years PAC has been successfully applied to investigate phase transitions [1, 2], defects in metals [3, 4], semiconductors [5–7], ceramics [8, 9] and intermetallic compounds [10, 11] and more recently to study binding sites in biochemical systems [12, 13]. The success of the method suggested that it can be applied to the investigation of a new and promising material class called MAX phases.

The $M_{n+1}AX_n$ (in short MAX) phases with $n = 1$–3 are nanolaminated ternary carbides and nitrides, where M is an early transition metal, A is a formerly called A-group element (mostly groups 13–14) and X is either carbon and/or nitrogen. These compounds have hexagonal symmetry and belong to space group D^4_{6h}, $P6_3/mmc$ (#194) with two formula units per unit cell. The three values of the index n lead to three different crystal structures: the 211 ($M_2A_1X_1$), the 312 ($M_3A_1X_2$) and the 413 ($M_4A_1X_3$) subclasses with the 211 phases representing the vast majority of these compounds [14, 15]. The transition metals form M octahedra with either carbon or nitrogen sitting in their center. The three crystal

configurations distinguish themselves only by the number of M-octahedra-layers which are embedded between two A layers.

The MAX phases possess an unusual set of properties: on the one hand, they behave like metals in terms of their remarkable machinability, damage tolerance, plasticity at high temperatures and their excellent thermal and electrical conductivity. On the other hand, they behave like ceramics in terms of their stiffness, low density, oxidation resistance, thermal stability and high decomposition temperatures [14–16]. This combination of characteristics makes them very interesting for industrial applications, e.g. as alternatives for nickel-based superalloys and for corrosion protective coatings [17–19], among many others. In the last decade many experiments with the MAX phases have shown that their mechanical properties are dominated by basal plane dislocations that in turn lead to kink bands and delaminations [20, 21]. Despite this knowledge many questions remain.

Perturbed γ–γ angular correlation spectroscopy is a particularly suitable tool to study materials on a sub-nanometer scale via hyperfine interactions to determine the short-range structure around the probe sites. This technique complements characterization with x-ray diffraction (XRD) and transmission electron microscopy (TEM). By using PAC, the electric quadrupole interaction between the quadrupole moment, Q, of the inserted probe nucleus and its own electron shell can be utilized to measure EFGs, which have been investigated herein for several 211-MAX phases.

The EFG is a traceless tensor whose components are the second spatial derivatives:

$$V_{ij} = \frac{\partial^2 \Phi(\vec{r})}{\partial x_i \, \partial x_j} = \begin{pmatrix} V_{xx} & 0 & 0 \\ 0 & V_{yy} & 0 \\ 0 & 0 & V_{zz} \end{pmatrix} \tag{1}$$

of the Coulomb potential $\Phi(\vec{r})$ at nuclear position with $|V_{xx}| \leq |V_{yy}| \leq |V_{zz}|$ after its diagonalization. The principal component, V_{zz}, is, in general, called the EFG and is related to the quadrupole frequency ω_Q by

$$\omega_Q \,[\text{Mrad s}^{-1}] = \frac{e\,Q\,V_{zz}}{4\,I(2\,I-1)\,\hbar}, \tag{2}$$

where e is the electron charge, Q is the nuclear quadrupole moment of the interacting spin state I and $\hbar$ is the reduced Planck's constant [4, 22]. The quadrupole frequency ω_Q is connected with the lowest, non-vanishing transition frequency of the split sublevels ω_Q^0 for half-integer nuclear spin by [22]

$$\omega_Q^0 \,[\text{Mrad s}^{-1}] = 6\omega_Q \,[\text{Mrad s}^{-1}]. \tag{3}$$

In general, one uses the spin-independent quadrupole coupling constant ν_Q (MHz), which is, in the present case, the utilized $5/2^+$ spin state, given by

$$\nu_Q \,[\text{MHz}] = \frac{e\,Q\,V_{zz}}{h} = \frac{20}{\pi}\,\omega_Q \,[\text{Mrad s}^{-1}]. \tag{4}$$

In addition to the strength V_{zz}, the asymmetry parameter

$$\eta = \frac{V_{xx} - V_{yy}}{V_{zz}} \tag{5}$$

is needed for the total characterization of the EFG and describes the deviation from axial symmetry. All hyperfine parameters such as quadrupole coupling constants ν_Q^i, their dampings δ_Q^i and their fractions f^i can be obtained from the perturbation function $R(t)$ [9, 23]:

$$R(t) = A_{22}^{\text{eff}} \sum_{i=1}^{m} G_{22}^i(t) = 2\,\frac{N(180°, t) - N(90°, t)}{N(180°, t) + 2N(90°, t)} \tag{6}$$

where A_{22}^{eff} is the effective anisotropy factor of the γ-ray emission cascade (see [24, 25] for anisotropy values of ^{111}Cd and ^{181}Ta), $G_{22}^i(t)$ the time differential perturbation factor and $N(\theta, t)$ the averaged number of coincidence spectra recorded at angles $\theta = 90°$ and 180°. In general for reasonable fitting of the data, m should be smaller than 5. The perturbation factor $G_{22}^i(t)$ is fitted by the equation [9]

$$G_{22}^i(t) = \sum_{n=1}^{3} s_{2n}(\eta^i) \cos[g_n(\eta^i)\omega_Q^i t] \exp[-g_n(\eta^i)\delta_Q^i t]. \tag{7}$$

For $I = 5/2^+$, the transition amplitudes s_{2n} and the coefficients $g_n(\eta)$ of the three transition frequencies $\omega_n = g_n(\eta)\omega_Q$ are listed and plotted in [26].

To interpret PAC results one has to know where the probes are located in the crystal. Often this can be a difficult task, especially for complex structures with different lattice sites. In the case of the MAX phases a few compounds exist in which this problem is easily solved, namely Ti_2InC and Zr_2InC. In both compounds it is reasonable to assume that the PAC probe used $^{111}In \rightarrow {}^{111}Cd$ resides at the 'natural' In lattice site since the isotope effects (radioactive ^{111}In and the constituent ^{115}In) have no influence on the chemistry. After implantation and the annealing of the lattice defects, the probes have to be located at the In-site in the structure. This systematic method with key compounds and the more general crystal class was already successfully demonstrated with the delafossites [27, 28]. The measured electric field gradients' strength and symmetry thus yield a signature for the In-site in particular, and the A-site more generally. The initial PAC experiments in Ti_2InC and Zr_2InC showed that this approach appeared to work [29].

In a similar way, the EFG of the M-site can be determined by using $^{181}Hf \rightarrow {}^{181}Ta$ probes in Hf-containing MAX phases like Hf_2SnC and Hf_2PbC. The compound Hf_2InC thus enables one to measure the M- as well as the A-site EFG by using both PAC probes. A prime example for this technique is the delafossite $AgInO_2$, which was studied by using ^{111}In (EC) ^{111}Cd and ^{111}Ag (β^-) ^{111} Cd as probes [27, 28].

Apparently the $^{111}In/^{111}Cd$ probes will most likely not occupy the X-site in the MAX phases due to structural reasons: one X atom sits in the center of each M octahedron and the M–X bond is the strongest and shortest one in the whole compound [14]. Furthermore the atomic radii of both In and Cd are more than twice as large as those of C and N. Due to the restricted space in the octahedra it is unlikely that the implanted impurities would replace the X atoms, which have even a different sign of the charge state.

Knowing the typical EFGs in the key compounds one is then able to identify the probe sites due to their EFG strengths

Table 1. Processing details and lattice parameters of the studied MAX phases. The time span of the applied temperature and load during syntheses is listed in the last column.

Phase	Reference	a (Å)	c (Å)	z	Temp. (K)	Load (MPa)	Time (h)
Ti_2InC	[61]	3.132[a]	14.060[a]	0.082[b]	1573	100	6–12
Zr_2InC	[62]	3.347[a]	14.910[a]	0.086[b]	1573	50	7
Ti_2AlN[c]	[63]	2.987[d]	13.611[d]	0.086[b]	1673	100	10
Cr_2GeC[c]	[64]	2.950[d]	12.101[d]	0.086[b]	1623	45	6
Nb_2AlC[c]	(This work)	3.106[d]	13.878[d]	0.086[b]	1873	35	10
Nb_2AsC	[65]	3.324[d]	11.904[d]	0.098[b]	1573	50	7

[a] Lattice parameters taken from [66].
[b] Taken from Springer Materials: the Landolt–Börnstein database.
[c] Compound made in a hot press.
[d] Lattice parameters taken from [44].

even in MAX phases which do not contain In or Hf. So the whole MAX family can, in principle, be investigated with the PAC technique to obtain information about the atoms and their local arrangement.

To confirm the allocation of the right probe site, some experimental results are compared with density functional theory calculations based on the 'augmented plane waves plus local orbitals' (APW + lo) method implemented in the WIEN2k computer code [30, 31].

2. Experimental details

The 211-MAX phases analyzed in this study were available as polycrystalline bulk samples. In all cases, the starting point was a set of pure metallic powders which were mixed in the right stoichiometric ratios with graphite, or in the case of Ti_2AlN with AlN. The resulting ball-milled mixtures were processed in two different ways: in one approach, the mixtures were vacuum-sealed in borosilicate ampoules and placed in a hot isostatic press (HIP). Alternatively the mixed powders were poured and wrapped in graphite foil, placed in graphite dies and mounted in a hot press (HP) applying an uniaxial load of approx. 45 MPa by means of a steel piston. The HIP chamber was heated up to 1673 K using a graphite furnace and pressurized with argon to a maximum pressure of 100 MPa. Details of the processing parameters are listed in table 1; additional information can be found in the cited references. After HIPing and cooling down, the glass was removed mechanically. The samples fabricated in the HP had to be cleaned from surface binary carbides that form due to a reaction with the graphite foil. The conditions listed in table 1 resulted in fully dense predominantly single-phase materials which were cut by a diamond saw and/or spark erosion into 10–20 mm^2 pieces that were 0.5–1.0 mm thick.

For the PAC studies about 10^{13} $^{111}In^+$ ions were implanted at 400 keV using the Göttingen heavy ion implanter IONAS [32, 33]. This isotope decays via electron capture with a half-life of 2.805 days to a γ–γ cascade to stable ^{111}Cd. During this decay the intermediate level with $I = 5/2^+$, $Q = 0.765(15)$ barn [34] and $T_{1/2} = 85$ ns is fed by emission of a γ-ray with 171 keV and depopulated by a 245 keV γ-quantum. This 245 keV intermediate state is used to measure the interaction with the EFGs.

The PAC measurements were performed with a standard planar four-detector set-up, where $2'' \times 2''$ NaI(Tl)-detectors were fixed in a 90° geometry. Coincidence spectra were recorded at measuring temperatures T_{meas} in the range of 10–1273 K and transformed to perturbation functions using the program SpectraPAC described in [35], which is available from [36]. Data analysis was performed with the program Winfit 3.0.4. [37] taken from the Division of Nuclear Solid State Physics, University of Leipzig.

For phase identification, x-ray diffraction patterns (Model D8 Advance, Bruker AXS) were taken before and after PAC measurements in a θ–2θ configuration, using parallelized copper Kα_1 radiation with a wavelength of 1.540 56 Å.

3. Results

3.1. Indium-containing MAX phases

3.1.1. Ti_2InC. In all cases, the PAC spectra directly recorded after implantation showed radiation damage, leading to a disordered local environment. Thus, the probes sensed many different local surroundings which led to a broad distribution of frequencies with $\langle \nu_Q \rangle \approx 150$ MHz and a large damping δ_Q, best seen in the Fourier transform in figure 1(a).

To anneal out the defects, the samples were sealed in evacuated quartz tubes ($p \sim (1 - 5) \times 10^{-5}$ mbar) to prevent oxidation and heated in a box-type furnace operating at different annealing temperatures, T_{ann}, from 573 up to 1373 K. After starting the annealing procedure, the crystalline structure began to recover. For Ti_2InC, the first changes in the $R(t)$ spectra already occurred after short annealing steps in the temperature range of 700–1000 K (cf figure 1(b)). A large fraction—of up to 80% of all probe atoms—sensed the same local surrounding, establishing an axially symmetric EFG of $\nu_Q = 17.3$ MHz, which is the known value for $^{111}In/^{111}Cd$ on a substitutional site in metallic In [38]. This provides unambiguous evidence for precipitates of metallic In within the Ti_2InC phase. Furthermore small In droplets of different size (0.25–75 μm) were formed on the surface of the samples during initial annealings (see figure 2). These droplets might be caused by a surplus of unreacted In in the material during its synthesis or eventually due to an incipient phase dissociation. The latter could be excluded, however,

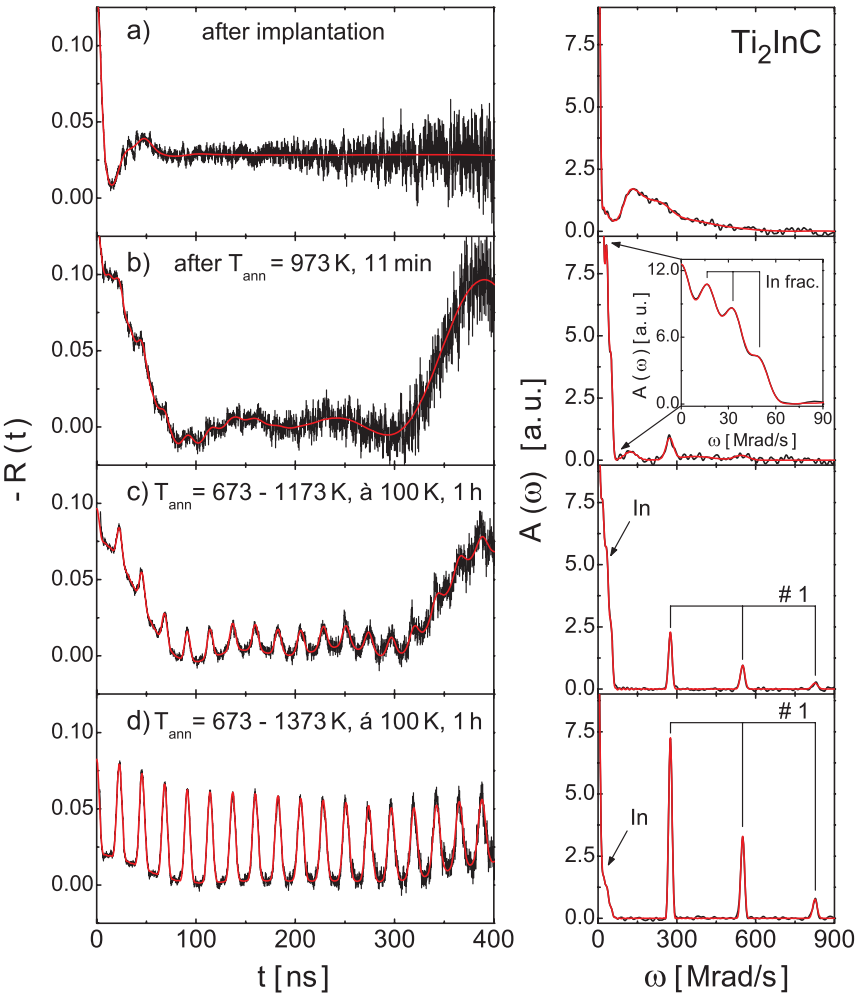

Figure 1. PAC spectra (left-hand side) and their Fourier transforms (right-hand side) for ^{111}In/^{111}Cd in Ti_2InC after various anneals. For the spectra in (c) and in (d), the samples were gradually annealed in 100 K steps from initial to final temperature shown in the figures. The time at each temperature was 1 h. The arrows in the FFT indicate the signal from probes in In metal, while the slider assigns the corresponding frequency peaks for probes residing at the A-site, labeled with #1.

since x-ray diffraction measurements showed already in the starting material pure In in the phase. The occurrence of In precipitates were discussed in detail in our previous PAC study [29].

Besides the fraction of probes present in metallic In, a second EFG was first found with a primary quadrupole coupling constant of about 287 MHz and a relative distribution width of $\delta_Q = \delta/\nu_Q = 3.5\%$ (figure 1(b)). This EFG became dominant after further annealing at 1173 K for 5 h (not shown) or after a gradual heating in steps of 100 K each carried out for 1 h up to 1073 K, see figure 1(c). The $R(t)$ curve was fitted using an axially symmetric quadrupole coupling constant of $\nu_Q = 292.0(6)$ MHz and a distribution width of 1.1(2)%. The fraction of probes which sensed this local surrounding was only about 25%. Since massive surface In precipitates appeared during the heat treatment (cf figure 2), which were removed manually afterward, it is reasonable to assume that the fraction of probes in In-metal would decline due to the In release, but still most of the probes resided in In clusters within the sample and were not embedded in the hexagonal MAX structure. During the three annealing steps below 1000 K—each taking less than 1 h—not only the unreacted A element was lost, but also a large amount (up to 20%) of the ^{111}In escaped from the sample and ended in the quartz tubes and in the precipitated In droplets. Further

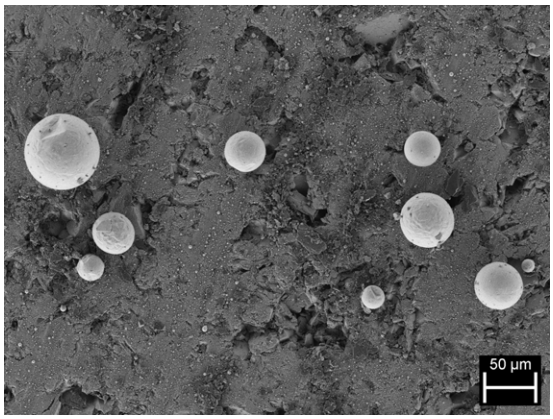

Figure 2. SEM micrograph of a Ti_2InC sample after heating at 773 K for 1 h in an evacuated quartz tube. The spheres on the surface belong to solidified In precipitates, which provide an indication of surplus In within the sample.

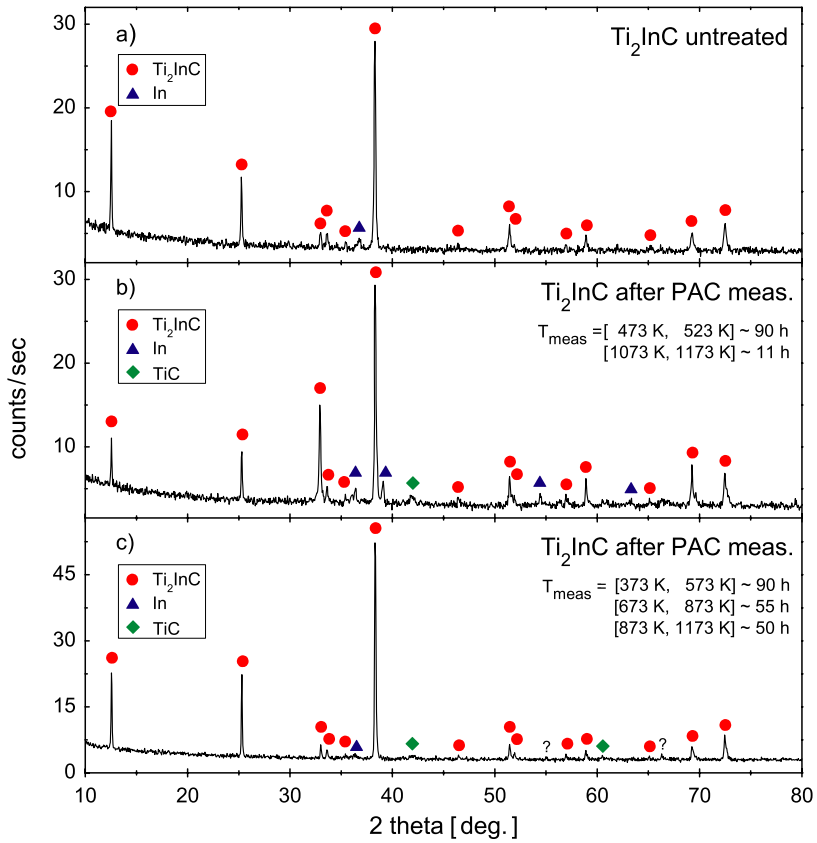

Figure 3. X-ray diffraction scans of Ti_2InC samples before and after the PAC measurements. The T_{meas} values shown on the right-hand side are the temperatures ranges, in which the sample was enclosed in quartz ampoules and heated in a furnace while the PAC spectra were simultaneously recorded for the stated times.

heatings caused no more In precipitates on the surface. The fraction of probes in metallic In could be reduced by further annealings up to 1373 K (cf figure 1(d)) to a minimum level of 20%. Below 1073 K this fraction was in the range of 50–70%, slightly varying for each individual sample. It was observed that the reduction of the fraction (i.e. $^{111}In/^{111}Cd$ in In) was mainly achieved at these high temperatures, while longer annealing times of several hours (typically 5 h) promoted the decline as well.

After long heatings of the order of approx. 195 h at temperatures between 373 and 1173 K it was observed that almost all the probes had diffused out of the metallic In precipitates and were associated with the lattice site characterized by a sharp EFG of $\nu_Q = 292.0(6)$ MHz. Therefore one has to conclude that, during the annealing cycles, unreacted metallic In was finally, for the most part, integrated in the MAX structure since no evaporated In in the form of droplets or metallic films were seen in the quartz ampoule at the end of the measurements. Consistent with this conclusion are XRD scans that showed an improvement in the phase quality after long anneals (compare the In signal in figures 3(a) and (c)). However, trace amounts of TiC were found after the long time anneals as well, proving that also a conversion of Ti_2InC to TiC_x may have occurred [39].

3.1.2. Zr_2InC. As mentioned above, the second key compound with In as a constituent element is Zr_2InC. Similar to the Ti_2InC samples, an appreciable In loss during the initial annealing steps was observed. The In formed small metallic droplets on the surface, which were manually removed before the next measurement. The PAC spectra showed that after 900 K for short annealing times (approx. 10 min) roughly 70% of the probes resided in metallic In clusters. A considerable change of the $R(t)$ curves, however, occurred after heating the samples above 1000 K for 5 h and beyond (not shown).

An almost identical $R(t)$ spectrum could be obtained by annealing the sample stepwise from 673 up to 973 K (figure 4(b)). After this treatment, the probe fraction in the In clusters decreased to 15(3)% and a clear axially symmetric ($\eta_1 = 0$) EFG appeared, having a quadrupole coupling constant of $\nu_{Q_1} = 344.1(5)$ MHz. This quadrupole frequency in Zr_2InC was roughly 50 MHz higher than the one found in Ti_2InC, but still of the same order of magnitude—a clear hint that the $^{111}In/^{111}Cd$ nuclei occupied the same lattice site in both phases. Looking closer at the Fourier transform in figure 4(c) one could find a second EFG ν_{Q_2} with a slightly lower frequency which merges in the first Fourier peak around $\nu_Q \approx 340$ MHz, but becomes more distinguishable for the second and third peaks at the twofold and threefold frequency distance, respectively. This second EFG was fitted with a coupling constant of $\nu_{Q_2} = 333.4(1.2)$ MHz, a relative damping of $\delta_{Q_2} = 0.7(4)\%$ and $\eta_2 = 0$. The ratio of the fractions $f_2(\nu_{Q_2} = 333.4\,\text{MHz})$ and $f_1(\nu_{Q_1} = 344.1\,\text{MHz})$ was $f_2/f_1 = 71(2)\%/14(3)\%$.

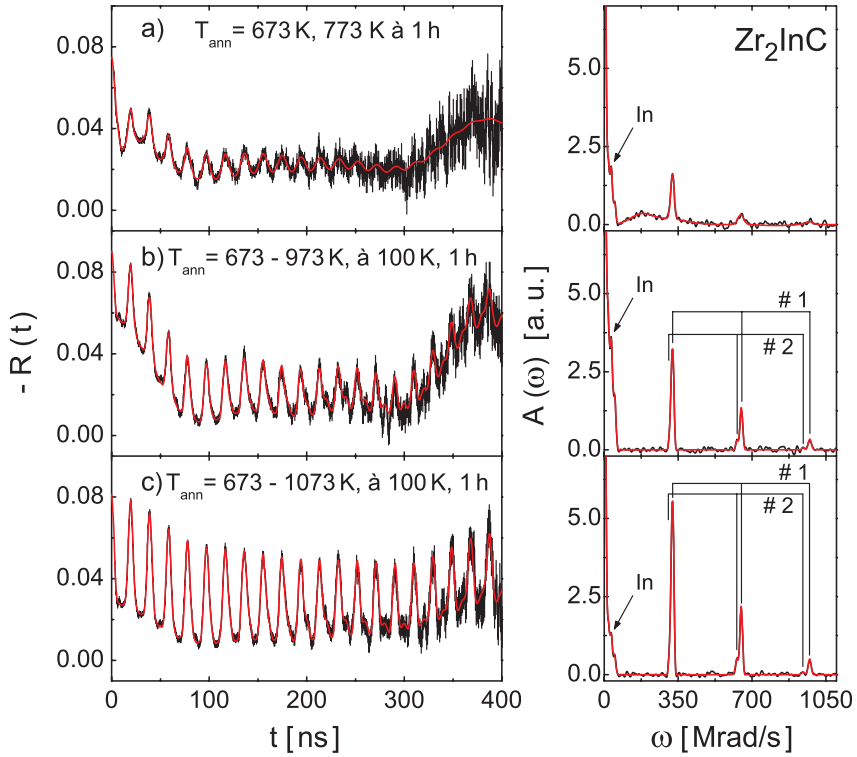

Figure 4. PAC spectra (left-hand side) and their Fourier transforms (right-hand side) for ^{111}In/^{111}Cd probes in a Zr_2InC sample after various annealing steps, which are noted in the figure. For all spectra, the specimen was gradually annealed in 100 K steps, each for 1 h, from 673 K to a maximum of 1073 K.

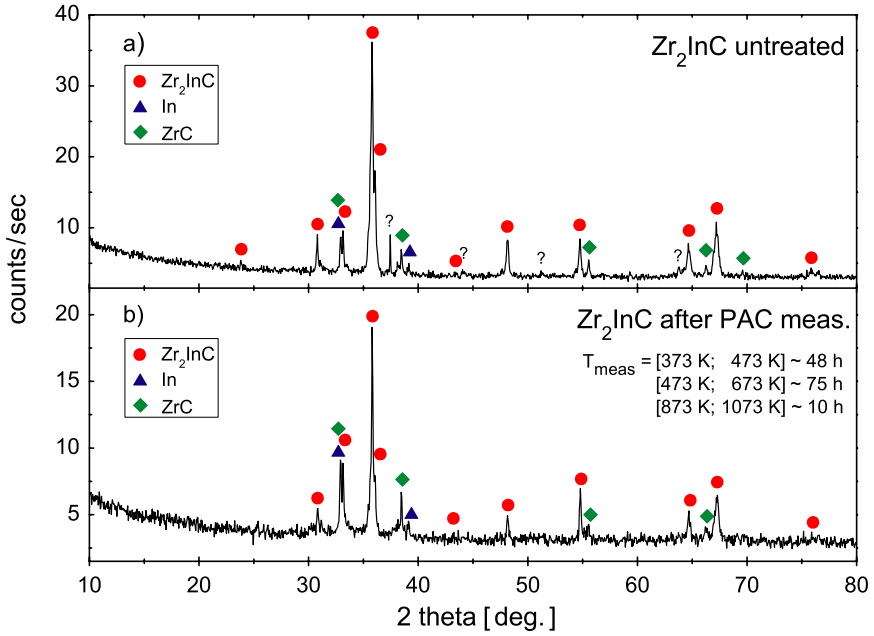

Figure 5. X-ray diffraction scans of Zr_2InC samples before and after the PAC measurements. The given T_{meas} values in (b) are the temperatures ranges, in which the sample was heated while the PAC spectra were recorded for the listed times.

The occurrence of two similar probe surroundings is a major difference to the Ti_2InC phase in which only one surrounding was observed after full annealing. Note that the percentage of the implanted ^{111}In residing in In precipitates in Zr_2InC was reduced to 15–20% at significantly lower annealing temperatures and shorter durations, which leads to the conclusion that the In at the grain boundaries of Zr_2InC is more mobile and either left the sample faster or was more easily incorporated in the MAX structure as compared to In in Ti_2InC. From XRD scans before and after the PAC

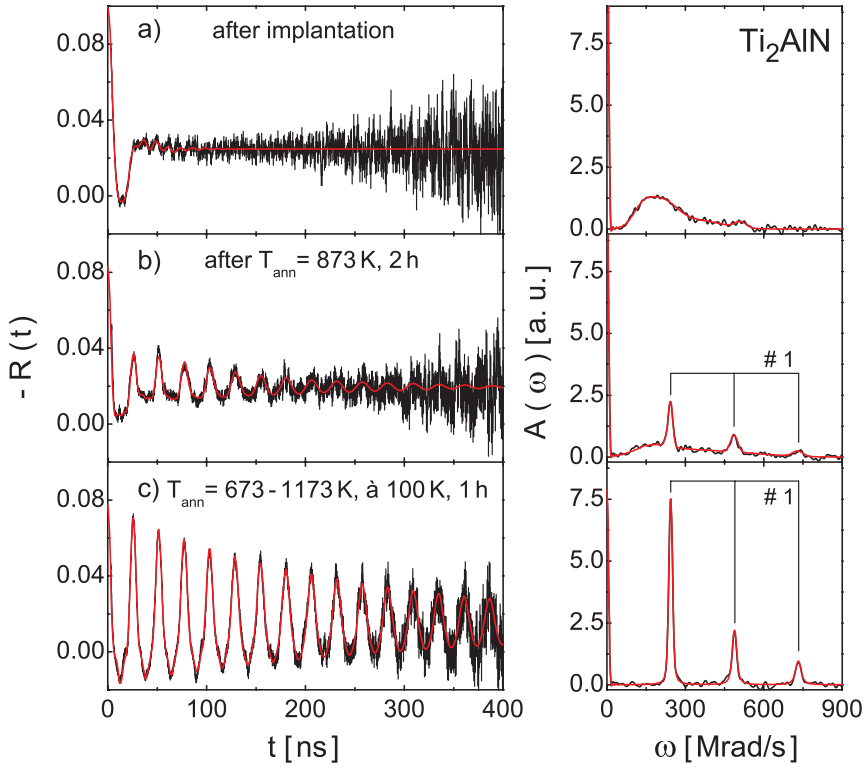

Figure 6. PAC spectra (left-hand side) and their Fourier transforms (right-hand side) for ^{111}In/^{111}Cd probes in Ti_2AlN after various annealing steps. Details about the annealing steps and durations are listed in the $R(t)$ plots.

measurements (see figure 5) it is difficult to obtain the right impurity amounts of In and ZrC at each time, since both main diffraction peaks lie at nearly the same position, i.e. $2\theta_{In} = 32.964°$ and $2\theta_{ZrC} = 33.040°$. However, the diffractogram in figure 5(b) shows pure In in the sample. This result is still consistent with the PAC experiments, even though the fraction of probes residing in pure In was about 15% after the quoted annealings (see treatment details in figure 5(b)) while the intensity of the main In/ZrC diffraction peak remains constant. But one has to consider that most radioactive probes were released from the bulk along with In agglomerations during the first annealing steps. This might be the reason why the major part of the remaining probes did not sense the local In-metal environment.

In general, a quantitative agreement between fractions in XRD and PAC is hard to obtain, as the ^{111}In-implantation range in our experiment is about 100 nm, whereas the x-rays from XRD can pass several micrometers and therefore lower lying ancillary phases can be detected as well. Unfortunately, no detailed data exist on the diffusion of In (inwards/outwards) in these samples at the applied temperatures.

3.2. Indium-free MAX phases

3.2.1. Ti_2AlN. The next step in understanding and interpreting the EFGs is to study MAX phases which do not contain In. The first compound selected was Ti_2AlN, since Al is in the same group as In in the periodic table. From a chemical point of view Al should be replaced by the implanted ^{111}In. One assumes that the probes, which occupy this lattice site, would sense an EFG of a similar strength as is observed in the In-containing MAX phases.

Already after annealing the samples at 873 K for 1 h an EFG with $\nu_Q = 259$ MHz (figure 6(b)) developed from the broad frequency distribution (figure 6(a)). This fraction increased rapidly, by successive 1 h heating in 100 K steps, reaching a maximum at 1173 K, where all probes sensed the same local surrounding (figure 6(c)). A closer view of this PAC spectrum and its Fourier transform (cf figure 6(c)) points to a texture within the sample [40]. The tapered $R(t)$ curve is a clear hint for a deviation from the polycrystalline structure, as well as the changed peak intensity ratio in the FFT. This ratio for polycrystalline materials (determined by the fixed values of the transition amplitudes s_{2n} and an ideal time resolution ($\tau = 0$ ns) of the spectrometer set-up [22]) is 2.6:2.0:1.0, but in the present case it is 7.8:2.3:1.0 for the sample aligned in plane. This texture may have been caused by the sample fabrication where the material was uniaxially loaded in the hot press.

The fit of the PAC spectrum in figure 6(c) gives a fraction of $f_1 = 100\%$ with an axially symmetric quadrupole coupling constant of $\nu_Q = 258.9(7)$ MHz and a damping of $\delta_Q = 1.3(3)\%$. Here the best fit to the data was achieved by using a Lorentzian damping type instead of a Gaussian damping otherwise.

Deviating from the In-containing MAX phases, in which a high probe fraction was located in metallic In precipitates,

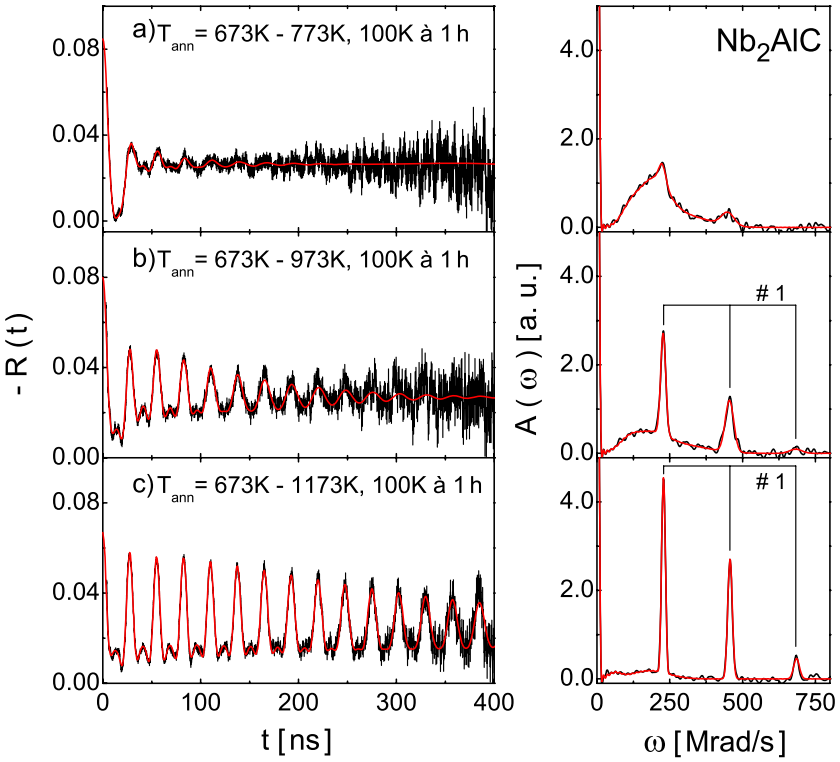

Figure 7. Annealing temperature-dependent PAC measurements of Nb_2AlC (left-hand side) and their corresponding Fourier transforms (right-hand side). The recorded spectra belong to the same sample, which was heated gradually in steps of 100 K for 1 h.

the PAC spectra for Ti_2AlN did not show any evidence for probes in pure Al. This is not surprising since Al clusters have never been reported in previous work. Had such clusters existed, an EFG with $\nu_Q^{Al} = 0$ MHz—due to the cubic crystal symmetry of Al—would have been observed. This would have led to an upward horizontal shift of the $-R(t)$ curve, which is not observed here. The other possibility that probes could reside in Ti grains—not seen with SEM or XRD either—the hexagonal Ti structure would generate an EFG with $\nu_Q^{Ti} = 27.8(2)$ MHz [41], which again was not observed. From the PAC studies described above it seems implausible that the probes reside on the M-site since the value of the quadrupole coupling constant is close to the ones found in Ti_2InC and Zr_2InC. The X-site in Ti_2AlN as a probe site is even more unlikely, just due to the different sign of the charge states of In and N, to name one reason.

To summarize, the only reasonable site for the ^{111}In probe atoms is the Al-site. However, the broadening of the transition frequencies could not be successfully fitted with a single Gaussian damping distribution but only with a Lorentzian damping function. One explanation is that the annealing was not fully completed, which might have led to a different broadening behavior.

3.2.2. Nb_2AlC and Nb_2AsC. As shown in section 3.2.1, it seems evident that the implanted ^{111}In ions reside at the Al-site. Up to this point only MAX phases with M elements from group 4 were studied with PAC. For further variation the phase Nb_2AlC is a suitable material to study the influence of the M element on the EFG (Nb belongs to group 5). X-ray diffraction scans, performed before the implantation, showed in all cases a high content of Nb_2AlC. Trace amounts of NbO_2, NbC_x and $NbAl_3$, described in detail in [42], could be found in a few samples as well. Reported evidence of Al_2O_3 grains [42] could not be identified with XRD nor PAC.

Similar to the annealing behavior observed in Ti_2AlN, short anneals at moderate temperatures were sufficient to achieve a probe fraction of about 80% on a specific local site, characterized by a sharp EFG at $\nu_Q = 242.4(6)$ MHz with $\delta_Q = 1.2(4)\%$ and $\eta = 0$ (figure 7(c)). This strength is quite close to the one found in the Ti_2AlN system and reinforces the statement that the radioactive nuclei reside on the A-site (here: Al-site).

Nevertheless approx. 35–45% of all probes sensed an average EFG of 80–100 MHz with a large distribution width of $\delta_Q = 30$–40%, it means that the local probe environments are not uniform, i.e. the lattice structure has not fully recovered (cf figure 7(b)). This led to a commensurable enhancement of the FFT curve with a maximum intensity of about 180 MHz. Due to its large δ_Q the asymmetry parameter η is not exactly definable, i.e. $\eta \approx 0.3$–0.5. This bump in the Fourier transform could be reduced by further annealings, even though a small heightening remained (cf figure 7(c)). The origin of this signal is most likely due to probes not residing at a specific lattice site, but distributed in a non-systematic order (e.g. interstitial sites) in the structure.

The clear EFG found in Nb_2AlC motivated us to investigate Nb_2AsC, in which Al is replaced by As. With As we have now a different chemical element at the A-site of the

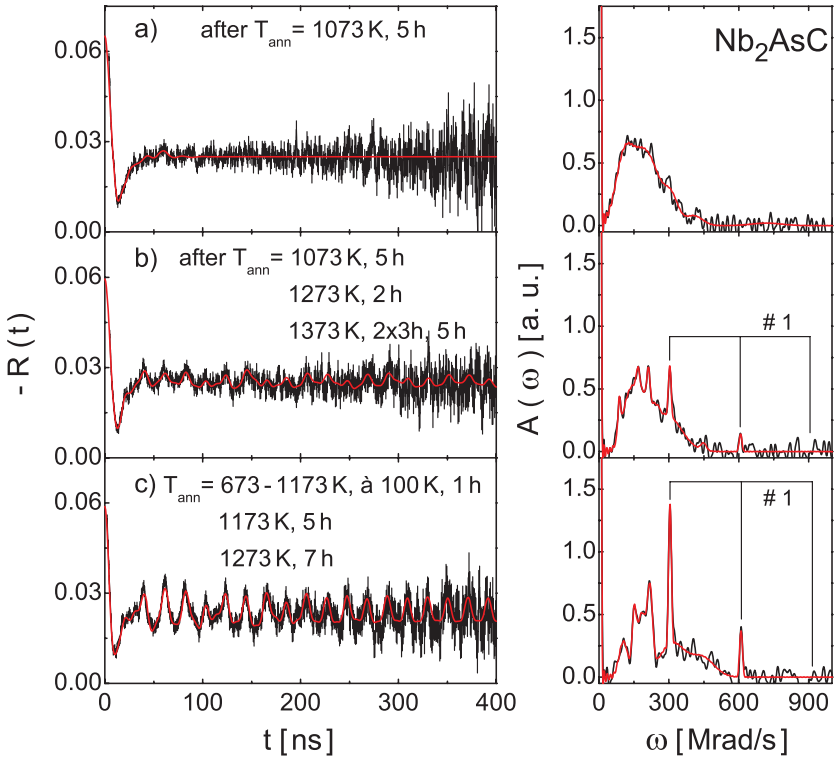

Figure 8. PAC spectra (left-hand side) and their Fourier transforms (right-hand side) of Nb_2AsC after long annealing steps at high temperatures. The label #1 indicates the corresponding frequencies for probes residing at the As-site.

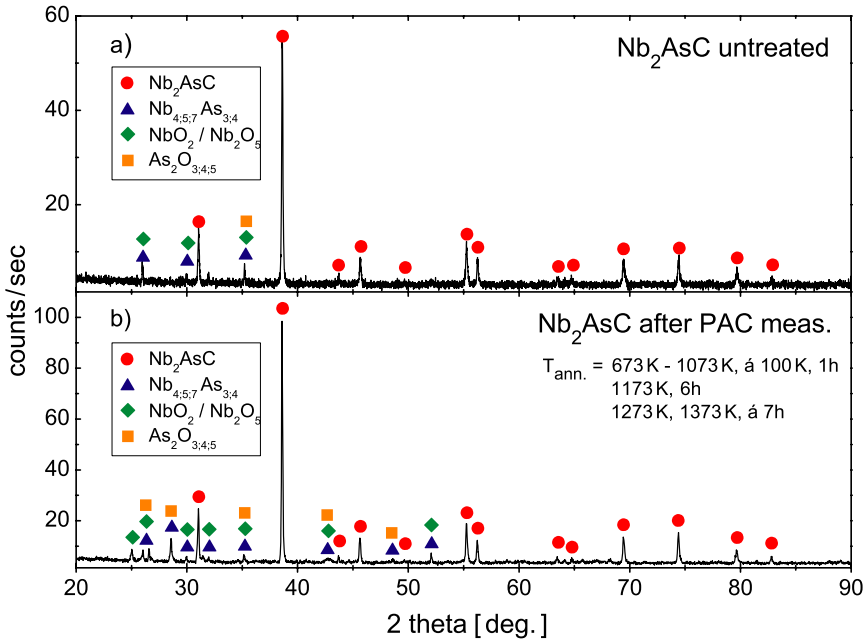

Figure 9. XRD patterns of Nb_2AsC before and after PAC measurements. The annealing steps (temperature and duration) which were carried out are noted in the lower plot. The diffraction peaks for the listed binary phases, e.g. Nb_4As_3, Nb_5As_3 and Nb_7As_4, are too close together to allow an explicit differentiation between them.

MAX compound, which belongs to group 15 instead of the previously discussed elements from group 13. So both M- and A-site elements are different than in the key compounds.

A series of measurements were carried out to find adequate annealing parameters to achieve a definite probe surrounding, comparable to the Nb-containing MAX phase described above. The best results (cf figure 8(c)), labeled with #1 were obtained after very long anneals at high temperatures. The maximum fraction of probe atoms sensing an EFG of $\nu_Q = 323(4)$ MHz with $\eta = 0$ was just about 10–15%.

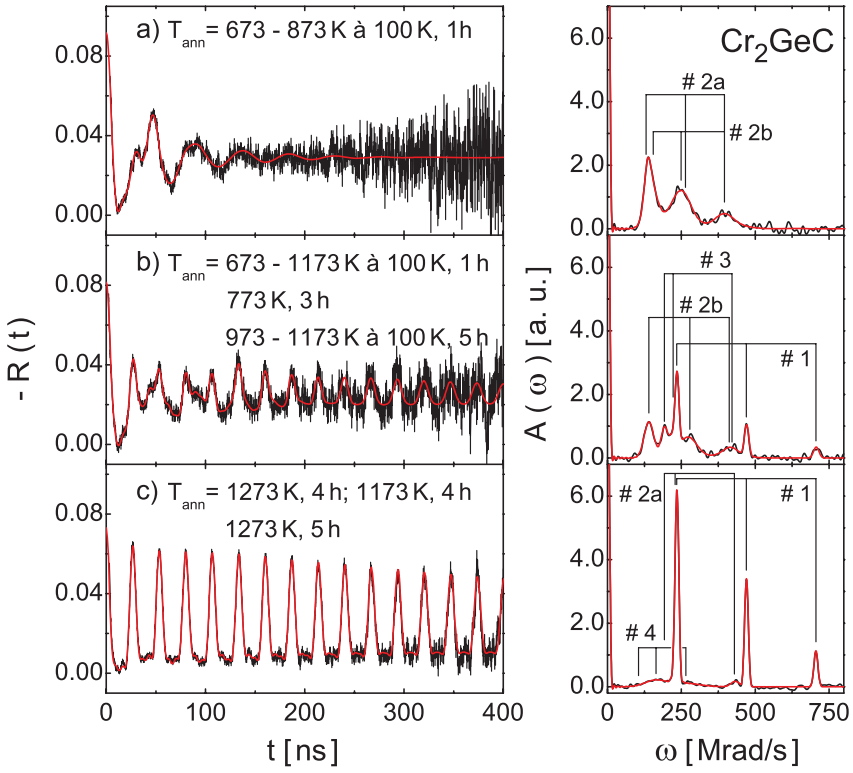

Figure 10. PAC spectra and their Fourier transforms for ^{111}In/^{111}Cd probes in Cr_2GeC after different annealings according to [40]. The annealing steps and durations are noted in the $R(t)$ plots. Spectra (a) and (b) belong to the same sample. The spectra (c) are obtained from another sample.

In other words the majority of the probe atoms induced due to their unspecific surroundings several broad frequency distributions about 110–150 MHz with δ_Q in the range of 10–20%. Comparing the strength of the observed EFG at 323(4) MHz to the ones found in other phases, one might assume that at least this percentage of the probe atoms ended up at the A-site (As).

A hint why this fraction is only 10–15% might be given by the lattice parameters of Nb_2AsC. While the length of the *a* axis—3.324 Å—is comparable to the ones of other MAX phases, see table 1, the *c*-axis is significantly shorter. The consequence could be a stronger interaction between the Nb and As layers, resulting in a tighter binding. This would explain the long annealing times and high temperatures as well as the difficulty in integrating the probes on the As-site. Another possibility is that the solid solubility of the radioactive probes is limited in this system due to size mismatches.

Moreover, the fairly high annealing temperatures resulted in a partial decomposition of the phase. Whitish precipitates at the edges of the samples grew as the annealing temperature was increased. XRD scans showed that As had formed several binary oxides, As_2O_{3-5}, which could be found within the sample as well (figure 9).

3.2.3. Cr_2GeC. Cr_2GeC was selected as a more crucial experiment to see whether the ^{111}In atoms are placed at the A-site. Because neither Cr nor Ge are chemically related to In, it is not obvious without the PAC measurements described above, at which lattice site the probes would reside.

Table 2. Fitting parameters for the Cr_2GeC PAC spectra shown in figure 10.

Figure	Label	Frac. (%)	ν_Q (MHz)	δ_Q (%)	η
10 (a)	#2*a*	60(10)	135.1(2.6)	14.2(5.6)	0.42(9)
	#2*b*	40(10)	138.8(5.5)	7.0(2.0)	0.19(8)
10(b)	#1	40(9)	249.9(9)	1.0(3)	0.0
	#2*b*	37(8)	145.4(3.4)	11.0(2.9)	0.15(10)
	#3	22(8)	130.8(3.6)	5.7(1.6)	0.80(13)
10(c)	#1	82(7)	249.6(5)	0.5(3)	0.0
	#2*a*	9(6)	135.9(1.3)	3.3(9)	0.82(7)
	#4	9(7)	90.4(5.7)	16.9(5.0)	0.46(21)

The performed PAC studies of ^{111}In in Cr_2GeC are discussed in [40], in which various annealing cycles were carried out. In most cases more than two fit fractions had to be used. Often, non-axially symmetric EFGs with $\eta = 0.15$–0.8 combined with an increased damping ($\delta_Q = 6$–16%) were observed (cf table 2). It is likely that the probes sensed an imperfect lattice environment (e.g. interstitial site) in Cr_2GeC due to the still present radiation damage which would also explain the large values of δ_Q. Alternatively, the probes may reside in binary phases, which were partially formed during the annealing process, as was seen by means of XRD.

By applying higher annealing temperatures for longer times, the probes sensed, in most cases, a unique local environment, figure 10(c), characterized by a well-defined EFG with $\nu_Q = 249.6(5)$ MHz, $\delta_Q = 0.5(3)\%$ and $\eta = 0$. Again, we conclude by comparing the strengths of the EFGs found above, with the one which belongs to fraction #1, that these probes reside at the A-site as well. However, a relic probe fraction with a broad distribution remains (figure 10(c)), which is responsible for the background in the Fourier transform.

Another observed axially symmetric EFG described in [40] with $\nu_{Q_2} = 148$ MHz was interpreted at first as a potential candidate for probes residing at the Cr-site. Due to the magnetic nature of Cr one could expect, had the probes occupied the M-site, that they might sense a magnetic hyperfine field (MHF). However, with PAC no magnetic behavior was observed, even at temperatures as low as 10 K. Furthermore no combined interaction of an MHF and an EFG was found. From this point of view, the experimental results allow us to conclude that the probes did not reside at the M-site which is additionally supported by DFT simulations that predict a very small EFG at the Cr-site (see computational results in table 4). The origin of this fraction, with $\nu_{Q_2} = 148$ MHz, is unclear at this time.

The annealing procedure of Cr_2GeC caused some difficulties. The increase of annealing temperature was strongly correlated with the loss of radioactive probes (see figure 11). Above 1000 K, over 25% of the present ^{111}In probes had evaporated from the samples, with increasing tendency. In analogy to previous studies of In-containing phases in which the loss was mainly induced by precipitation of excess In, grayish colorations inside the quartz glass tubes were observed in the present case. To date, we are not sure whether these discolorations are due to the evaporation of unreacted Cr/Ge or due to decomposition products of Cr_2GeC. XRD scans before PAC [40] showed no evidence for unreacted pure metals. Furthermore it is not proven, whether a supposed release of Cr or Ge would coincide with a loss of ^{111}In.

Another possibility is that the In loss was due to the porous character of the spark eroded Cr_2GeC slices, see figure 1 in [40]. The large inner surface would enhance the possibility for ^{111}In to diffuse out, especially due to the fact that the melting point of In of 430 K [43] is low in comparison to the applied annealing temperatures. However, experiments with samples, which were diamond cut and finely ground, exhibited the same features. This might show that the In loss is a general issue, presumably caused by a temperature-driven diffusion mechanism.

To prevent a precipitation of the probes during annealing, a small piece of inactive ^{115}In was inserted in one ampoule to provide an In-backpressure and thus slow down evaporation of the probe ^{111}In. But after annealing for 2 h at 1273 K more than 90% of the current activity was localized in the attached In piece. Additionally a large amount of ^{115}In had diffused into the sample. Furthermore, 80% of the remaining ^{111}In resided in the incorporated In-metal within the sample, as shown by an EFG of $\nu_Q = 17.3$ MHz.

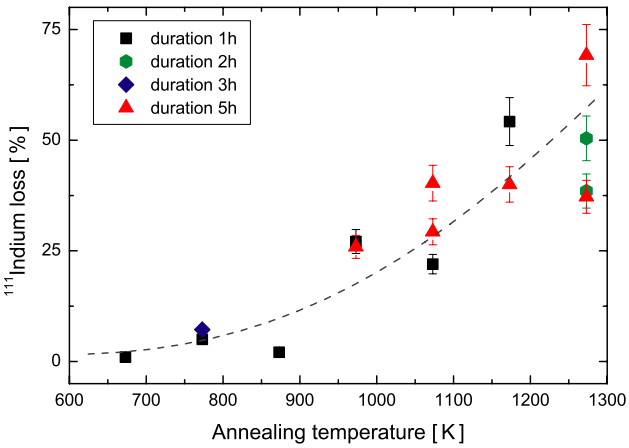

Figure 11. ^{111}In loss in Cr_2GeC. The activity of the tubes were measured in each two-sided case (implanted side and reverse) by a β–γ contamination ratemeter, once containing the sample and once without it. The counting rate deviation was estimated with 5% for each reading.

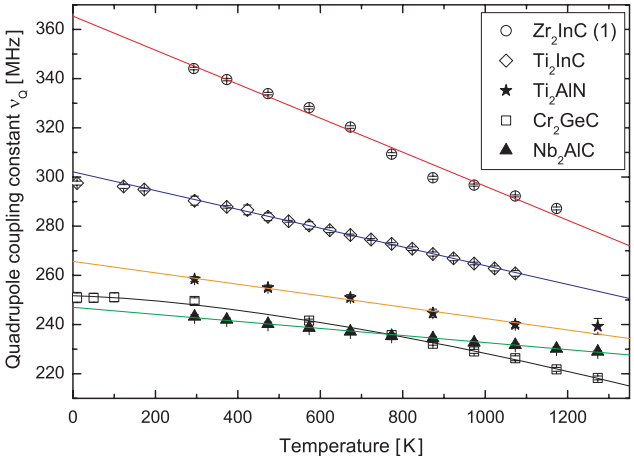

Figure 12. Effect of temperature on the quadrupole frequencies ν_Q of several MAX phases. The parameters $\nu_Q(0)$ and a were obtained from fitting the data in the range of RT to 1273 K by means of equation (9) and are listed in table 3. By taking the low temperature data points of Cr_2GeC into account, the $T^{3/2}$ law (equation (8)) results in good agreement with the frequency course. For Ti_2InC, only the linear fitting function matches the whole data set.

3.3. Temperature dependence of the EFGs

With the exception of Zr_2InC—with two well-defined EFGs—and Nb_2AsC, all the other annealing experiments described above resulted in a single, sharp EFG of comparable strengths that were attributed to In/Cd probes residing at the A-sites. To investigate the influence of temperature on this probe surrounding, the annealed samples were sealed into evacuated quartz ampoules and placed in a BN furnace.

Since the MAX phases are known for their high temperature stability [14, 44], a large temperature range was used for the PAC measurements. In many non-cubic metals a $T^{3/2}$ dependence of the EFG was found [45], described by the

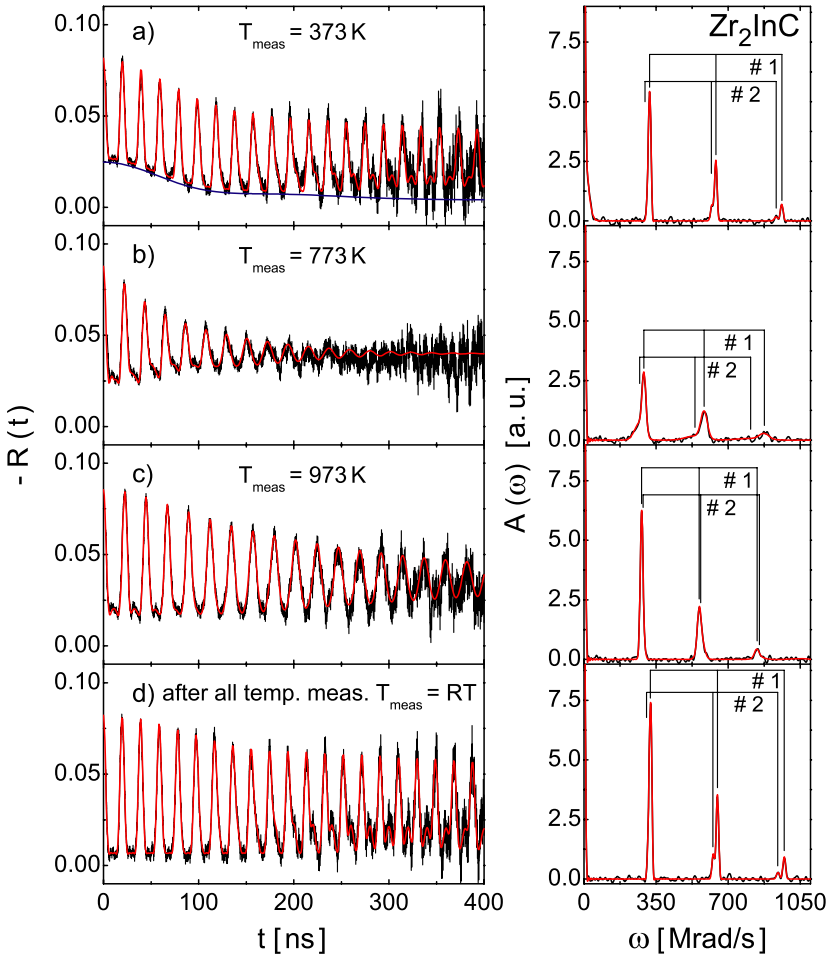

Figure 13. Temperature-dependent PAC measurements of an annealed Zr_2InC sample (annealed from 773 to 1073 K in steps of 100 K, each lasting for (1 h), heated from RT to 1173 K in 100 K steps. The blue line shown in spectrum (a) indicates the probe fraction in metallic In near the In melting point.

relation

$$\nu_Q(T) = \nu_Q(0)(1 - B\,T^{3/2}). \tag{8}$$

The reason for the $T^{3/2}$ behavior can be related to lattice vibrations. One hypothesis is that this temperature dependence is caused by the mean square atomic displacement of the lattice components, which, in the Debye model, is proportional to T^2 at low temperatures and is linear with T at higher temperatures. This leads to a $T^{3/2}$ response over the entire temperature range [22].

In the present study, instead of the $T^{3/2}$ dependence, a linear decrease of the quadrupole coupling constants ν_Q in the temperature region from 293 to 1273 K was observed for all compounds (cf figure 12). The simplest interpretation of this result is that the decline of the EFG strength is due to thermal lattice expansion. Consequently the quadrupole coupling constant values were fitted using the equation

$$\nu_Q(T) = \nu_Q(0)(1 - a\,T). \tag{9}$$

According to equation (9), the parameter $\nu_Q(0)$ is the extrapolated quadrupole coupling constant at $T = 0$ K, determined by fitting the data in the region between 293 and 1273 K. The fitting variable a describes the normalized linear decrease of ν_Q and was calculated for each compound, except for Nb_2AsC, in which only a small fraction of probes were located at the A-site after the various annealing procedures.

Table 3. Linear fit results of the quadrupole coupling constants ν_Q for annealed samples in the temperature range from 300 to 1300 K. The normalized decrease a of ν_Q is compared with the thermal expansion coefficients, α_{av}, taken from [44], if available.

Phase	$\nu_Q(0)$ (MHz)	a (10^{-5} K^{-1})	α_{av} (10^{-6} K^{-1})	a/α_{av}
Ti_2InC	302.1(6)	12.6(4)	—	—
$Zr_2InC(1)$	365.4(4)	18.9(3)	—	—
Ti_2AlN	265.7(1.2)	8.7(7)	10.3(2)	8.5(7)
Cr_2GeC[a]	251.7(4)	12.5(4)	14.5(2)	8.6(3)
Nb_2AlC	247.0(5)	5.8(4)	8.1(2)	7.2(5)

[a] $\nu_Q(0)$ was determined by applying the $T^{3/2}$ law while the parameter a was derived from the linear fit using the high temperature data.

A linear fit describes all the data from RT to 1273 K. Two phases were also measured down to 10 K. Including these additional data points, the entire frequency course of Cr_2GeC

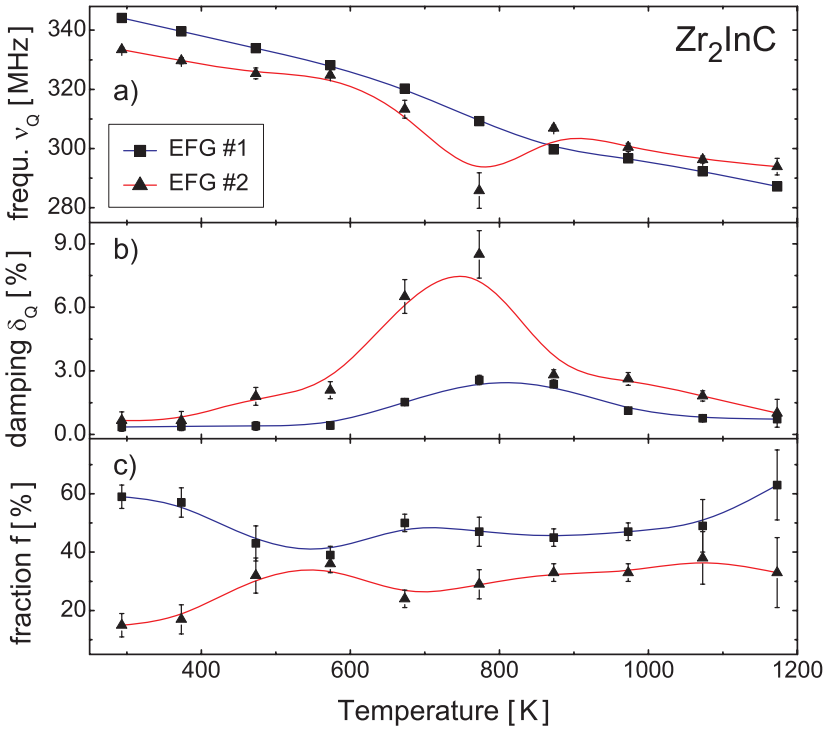

Figure 14. Temperature dependence of hyperfine parameters in Zr_2InC. The sample was chronologically heated in steps of 100 K, increasing from RT to 1173 K. The notation for the EFGs #1 and #2 is according to figure 4. The missing fraction to 100% corresponds to probes in liquid In metal (i.e. 26(3)% at RT, decreasing to 5(4)% at 1173 K).

could also be fitted using the $T^{3/2}$ law from equation (8) (shown in figure 12). For Ti_2InC, no $T^{3/2}$ dependence was found—the fit did not match with the data, even not after including the low temperature results. Alternatively, one could fit the data in the region of 10 and 293 K by assuming a very small a. The observation that the EFG remained nearly constant below RT indicates that the changes of the structural and the electronic properties do not affect the charge distribution of the Cd electron shell.

The a values were compared with the average thermal expansion coefficients α_{av}, obtained from high temperature x-ray diffraction experiments [44]. In that reference it was reported that the coefficients α_{av} varied from 5.5×10^{-6} K^{-1} (Nb_2AsC) to 14.5×10^{-6} K^{-1} (Cr_2GeC). The PAC results show a similar trend (see table 3). This is best seen by noting that the nondimensional ratio a/α_{av} is around 8 for all compositions tested herein. So far no experimental α_{av} values for the In phases exist. Further temperature-dependent PAC studies of Cr_2AlC, Ti_2AlC and V_2AlC are in progress to confirm this assumption and will be published in the near future.

While the A-site PAC parameters in the phases Ti_2InC, Ti_2AlN, Cr_2GeC and Nb_2AlC did not show any anomalous changes in the temperature range from RT to 1273 K, a different behavior in Zr_2InC was observed (see figures 13 and 14). As discussed above, the PAC spectra of this compound were fitted with two very similar EFGs, cf figure 13(a) and table 5, both having a small damping width of 0.4–0.7% at RT. In addition, the EFG caused by the fraction of ^{111}In in metallic In precipitates (ν_Q(RT) = 17.3 MHz) was also determined. The latter signal starts to disappear at about 375 K, close to the In melting point (see blue curve in figure 13(a)). Needless to say, this result indirectly confirms that this signal is associated with probes in metallic In.

The $R(t)$ spectra in figures 13(a) and (d) prove the existence of a small fraction of EFG #2 (ν_{Q_2} = 333.4(1.2) MHz), seen in the $R(t)$ curves for $t > 250$ ns and in their Fourier spectra as a tiny bump in front of the second peak around 650 Mrad s^{-1}. Figure 14 shows the development of the PAC parameters ν_Q, δ_Q and their fractions f with increasing temperature. The fractions f_1 and f_2 (figure 14(c)) can be interpreted as nearly two mirror-inverted lines over the whole temperature range. In the region between 600 and 900 K the damping width increases: δ_{Q_2} reaches its maximum of 8.5(1.2)% at 773 K, while the maximum value for δ_{Q_1} is 2.6(3)% (figure 14(b)).

At higher temperatures the dampings decline to their initial values. Since these changes were observed upon heating and cooling of several Zr_2InC samples, it is reasonable to conclude that they are both reversible and reproducible. Searching for a similar behavior in other PAC experiments, one finds that, in the intermetallic phases such as $TiPd_2$ [46], $HfAl_2$ [47] and Ti_2Ag [48], a reversible increase of the damping is associated with a probe switching its lattice site. Here we see a 'switching' between two similar EFGs, which points to a dynamic process showing a small fluctuating charge in the near-neighborhood of the probe.

The crossover of both quadrupole coupling constant curves at approx. 900 K (figure 14(a)) is proven by the

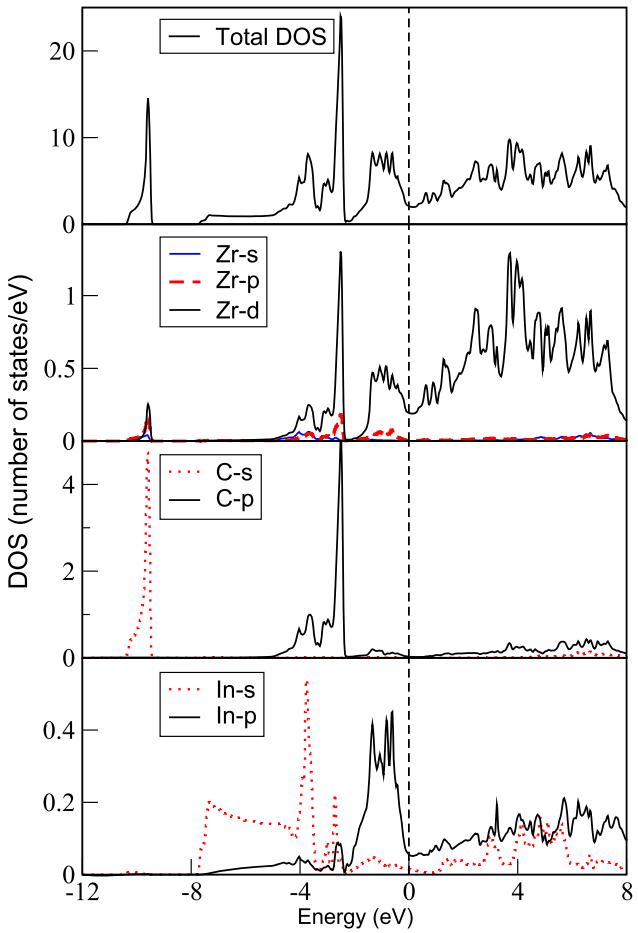

Figure 15. Total and partial density of states (DOS) for the compound Zr_2InC. The Fermi level is located at zero of the energy scale. Clearly noticed in this figure is the formation of hybrid states formed from the Zr-d, C-p and In-p states.

Fourier transforms of the corresponding $R(t)$ spectra, which were recorded above 873 K. These show that the peaks in the twofold frequency distance feature a weaker trailing edge from the right instead of the left for FFTs below that temperature (cf figures 13(b) and (c)). This can be taken as evidence that the strength of EFG #2 increases compared to EFG #1 while the fraction is still smaller than EFG #1.

While the values for the coupling constants and dampings show a temperature reversibility, this is not the case for the fraction of probes in the In clusters. Starting at RT, about 26(3)% of all probes reside in In-metal (see annealing details in the caption of figure 13). During the first heatings up to 773 K this fraction remains constant, but starts to decrease rapidly at 973 K and nearly vanishes after the whole heating cycle, as shown in figure 13(d). This fact can be explained by a selective sublimation of In, observed in this study around 1000–1200 K. Such a behavior is reported, for example, for the Ti_2InC system at about 1073 K [39, 49]. In the present case, some In droplets were found at the head of the Zr_2InC-containing ampoule after the temperature measurements, while no In accumulations had been noticed in the ampoule containing Ti_2InC after a similar procedure.

4. Details of the calculations

The simplest approach to calculate EFGs is the point charge model (PCM) in which the charges are assumed to be point-like and localized at the nucleus' position. However, the PCM is mostly used for complete ionic systems (e.g. in metal oxides [50]), in which the atoms have well-defined charge states. This is not the case for the MAX phases. Here, the M–M bonding has a pure metallic character and the M–X bonding is predominantly covalent with a small ionic contribution [14]. Therefore it is not surprising that the PCM cannot provide reliable results, which leads us to utilize a different method, described in section 4.1.

4.1. Density functional theory calculations

4.1.1. Exemplary simulation details for the compound Zr_2InC. *Ab initio* calculations of the EFGs were performed in the framework of density functional theory (DFT) [51–53] by using the augmented plane waves plus local orbitals (APW + lo) method, which is implemented in the WIEN2k package [54, 55]. To compute the exchange and correlation functionals, the generalized gradient approximation (GGA) of Perdew, Burke and Ernzerhof was utilized [56]. The number of plane waves was limited to $K_{max} = 7/RMT_{min}$, where the adopted muffin-tin radii (RMT)—defining the region where atomic orbitals (inside the sphere) and plane waves (outside the sphere) are applied—were 2.23, 2.50, 2.50 and 1.98 a.u. for Zr, In, Cd and C, respectively. It defines the cutoff for the energy of the plane wave representation of the wavefunctions (wf) at the interstitial region as $E_{max}(wf) = 12$ Ryd.

The charge density was Fourier-expanded up to $G_{max} = 16$ (i.e. E_{max}(potential) = 256 Ryd) and—for the Brillouin zone integrations—a tetrahedral mesh of 1000 k-points was used for the case of the Zr_2InC unit cell comprising eight atoms. To simulate the effect of Cd substituting for In in Zr_2InC, a supercell with 32 atoms was utilized. In this case the unit cell was doubled twice along the a and b axes, taking the experimental lattice constants from [14]. Due to the high c/a ratio, of about 4.46 [14], a multiplication along the c axis was not required. One of the A-layer atoms within the supercell was substituted by a ^{111}Cd probe atom. The number of k-points within this cell was set to 120. In the first step of the calculations it was observed that the theoretical volume—within the approximations—agreed with the experimental one for Zr_2InC to less than 0.5%. Additionally a variation of the c/a ratio was carried out and again only a slight mismatch with the experimental data of less than 1% was found. In a third step, the internal parameter z describing the position of the Zr atoms within the unit cell was relaxed and changed to 0.082 65 as compared to the experimental value of 0.086 (see table 1). Finally calculations were performed on the supercell, wherein one In atom was replaced by a Cd atom. In this case only atom relaxations, within this larger cell with the experimental lattice parameters, were applied. The results of these calculations are shown in figures 15–17 as several plots of the density of states.

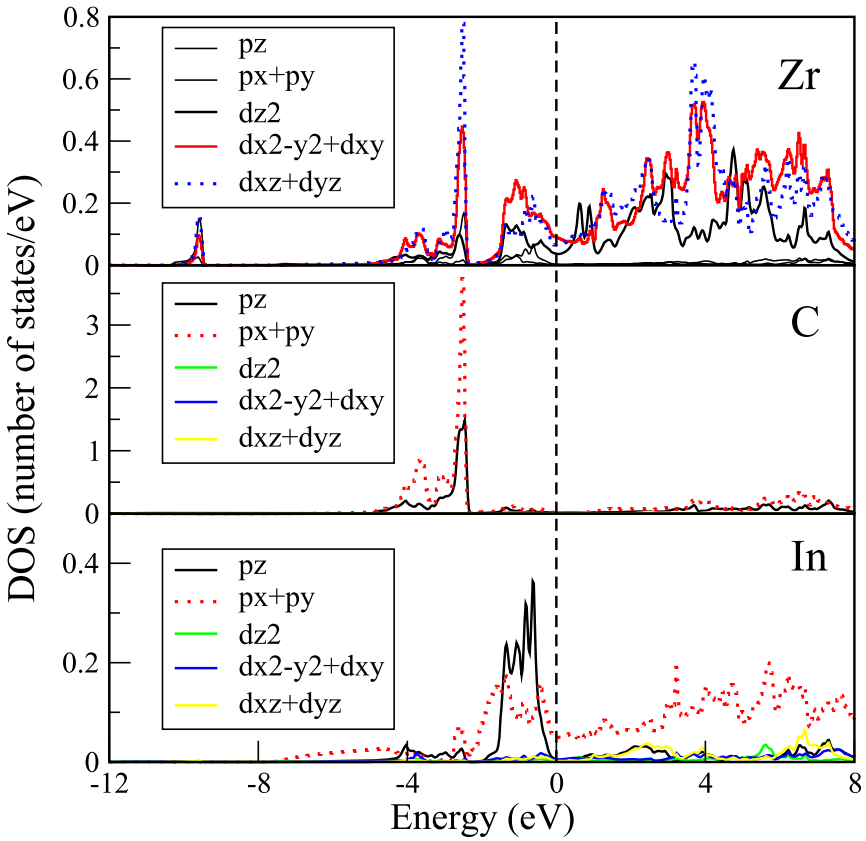

Figure 16. The Zr, C and In density of states projected along the respective p and d wavefunctions. The Fermi level is located at the zero of the energy scale. The difference in electronic populations of the In p_z and In $(p_x + p_y)/2$ is responsible for the appearance of an electric field gradient at In nucleus (see text). The In p_z and the C $(p_x + p_y)$ form a hybrid state with the Zr d states, mainly with Zr $(d_{x^2-y^2} + d_{xy})$ and Zr $(d_{xz} + d_{yz})$ states, respectively.

The resulting EFGs, in units of 10^{21} V m^{-2}, are -27.543, 4.695, 0.237 and -20.172, for the In, Zr, C and Cd atoms, respectively. All of these EFGs are axially symmetric, i.e. $\eta = 0$, due to symmetry constraints.

4.2. Influence of the Cd foreign atom at the In-site in Zr_2InC

According to the electronic structure calculations, we conclude that Zr_2InC is metallic in character as seen from figure 15. The largest electronic density at the Fermi level is due to the Zr 4d states, followed by the In 5p states. The Zr 4d states form hybrid orbitals with the C 2p and In 5p states resulting on covalent bonds between Zr and C, as well as between Zr and In [57, 58], as seen in figure 15. There are no direct interactions between the C and In atoms. The C s electrons lie deeply within the valence region, at approx. -10 eV under the Fermi level and do not participate in the binding of the Zr_2InC structure. A similar situation occurs with the In s electrons, although they do have some interaction with the C 2p states around the energy range of -8 to -2 eV and with the In Zr hybrid in the 0 to -3 eV range. The EFG at the In nucleus is almost exclusively (≈98%) caused by its 5p states. The remaining small contribution is due to its 4d shell, since it is not completely filled. The large 5p contribution to the In-EFG is due to the non-symmetrical filling of its p_z and

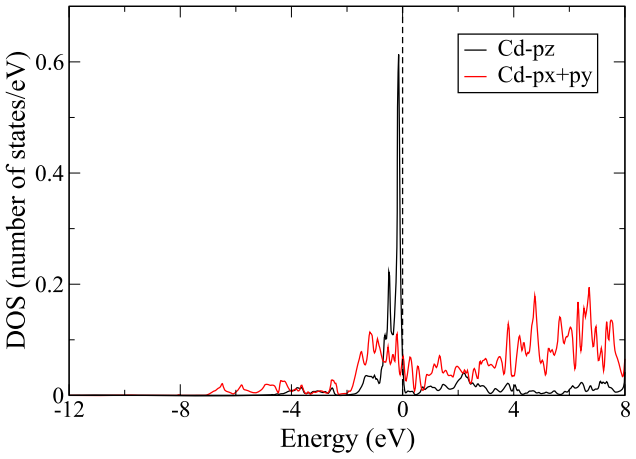

Figure 17. Projected density of states of a Cd impurity substituting for In in Zr_2InC among its p wavefunctions. The Fermi level is located at the zero of the energy scale. The difference in electronic populations of the Cd p_z and Cd $(p_x + p_y)/2$ is responsible for the appearance of an EFG at Cd nucleus (see text). It is also seen the increase of the localization of the Cd p_z as compared with the In p_z (figure 16).

$p_x + p_y$ sub-shells. The In p_z orbital is mainly responsible for the In Zr covalent bond, as observed in figure 16, where it is seen that the In p_z states are those which form the hybrids

with the Zr 4d states. On the other hand, the In p_x and In p_y form the In–In bonds within the x–y plane. The number of electrons occupying the p_z sub-shell is 0.294 while the $p_x + p_y$ sub-shell appears with 0.3260 electrons, resulting in an asymmetric filling as given by $p_z - (p_x + p_y)/2 = 0.13$, and is responsible for the appearance of a large net EFG at the In nucleus, while the EFG is oriented along the [001] direction.

When Cd replaces In, only minor changes occur to the whole valence electronic structure. The decrease of the electronic density is the most evident. A small localization of the Cd p_z states is shown in figure 17 as the corresponding peak in figure 16 is somewhat broader, suggesting that the Zr–Cd bond is weaker than the Zr–In bond. At the Cd-site, the new electronic populations at its p states is $p_z = 0.189$ and $p_x + p_y = 0.176$, giving $p_z - (p_x + p_y)/2 = 0.10$. The reduction of this asymmetry factor on electronic populations from 0.13 to 0.10 in going from In to Cd is responsible for the reduction of the magnitude of In-EFG (i.e. −27.543) to the Cd-EFG (i.e. −20.172). The minus sign of the EFG is a consequence of the larger charge density being located on the p_z orbital, originating from a prolate charge distribution around the main z axis.

Therefore, it is plausible to suppose that for the case, where Cd substitutes for an A-site atom in compounds like Ti_2InC, Ti_2AlN, Cr_2GeC and even other 211-MAX phases, the only changes in relation to the Zr_2InC case is the electron population of the Cd-p sub-states, giving rise to different EFGs just due to the different relative electron concentrations on its p_x, p_y and p_z orbitals.

4.3. Influence of the Cd foreign atom at the M-site in the studied MAX phases

Calculations were also performed for the cases when a Cd atom substitutes the M-site within the studied MAX phases and the results of the obtained EFGs are also presented in table 4. For these cases, 3 × 3 × 1 supercells were utilized since Cd possesses largely different electronic structures as compared with Ti, Zr and Cr. Again, the atomic structures were relaxed until the forces on the atoms were smaller than 1 mRyd/a.u.

Relatively large atomic displacements were observed for these cases. The Cd atom displaces away from the nearest-neighbor N atoms in Ti_2AlN, and from the C atoms in Ti_2InC, Zr_2InC and Cr_2GeC, respectively, by 0.45 Å, 0.27 Å, 0.22 Å and 0.31 Å. As a consequence the Cd atoms also move towards Al, In, In or Ge, respectively, in Ti_2AlN, Ti_2InC, Zr_2InC and Cr_2GeC. These displacements affect the degree of the small electronic population of the Cd-p states due to the interaction with the Al, In, Ge, N and C p states and also affect the observed EFG on Cd. This effect can be visualized in the DOS plots of figure 18, where it is shown, for comparison, the projected DOS on Cd p, Al p and N p states for Cd occupying the Ti-site in Ti_2AlN. In this figure one sees that the Al p states are located around −2 eV while the N p is around −5 eV. The upper curves of figure 18 correspond to the Cd p states. It can be noticed that both the Al p and N p states transfer some charge to the Cd p states and, moreover, the Cd

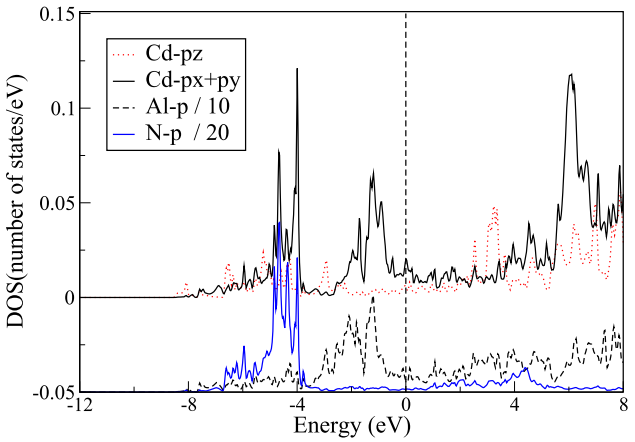

Figure 18. Density-of-states plots of the Cd p, Al p and N p for Cd substituting for Ti in Ti_2AlN. The two upper curves correspond to Cd while the curves at the bottom correspond to N and Al which were also scaled down (by the factors shown) and shifted for clarity. Clearly seen is the different influence of the (N, Al) p states on Cd p_z and Cd $(p_x + p_y)$.

$p_x + p_y$ is more affected than the Cd p_z state. This imbalance is sensed by means of a presence of a net EFG at the Cd nucleus. Similar effects are seen for all the cases studied. Since the population of $p_x + p_y$ is larger than that of the p_z states, the EFG is positive in this case. The effect is larger in the case of Ti_2AlN as compared to the other cases, as seen from the values of EFG in table 4. It should be mentioned that the amount of transferred charge to the Cd 5p states, as seen from the total charge inside the Cd *muffin-tin* spheres, is very small, being 0.10, 0.03, 0.36 and 0.21 electrons, respectively, for the Ti_2AlN, Cr_2GeC, Ti_2InC and Zr_2InC. Although being small, the charge transfer can be considered a real feature within the present approximations.

Also interesting to note is the behavior of Cd d states. In the cases where the EFG is small, for instance, the cases where the X atom is a C atom (see table 4), we observe only small overlapping of Cd d states with the neighboring atomic states, as shown from the fact that they retain the atomic character. This is especially true for Zr_2InC since several of the Cd d orbitals present quite undisturbed atomic character. In contrast, the case of Ti_2AlN present all the Cd d states largely dispersed in energy, indicating larger interaction with the other atoms within the lattice. This case also presents larger Cd p dispersion as seen in figure 18, larger Cd dislocations and larger Cd EFG.

These effects cannot be well correlated with the relevant atomic distances. While the Cd–Al distance in Ti_2AlN is smaller than the corresponding distances in In-containing MAX phases, which could increase the Cd–Al interaction and the Cd-EFG, the distance between Cd and Ge in Cr_2GeC is even smaller but the effect decreases. The same argument can be applied to the Cd–N or Cd–C distances: the Cd–N distance in Ti_2AlN is the largest among the studied compounds and the effect of the Cd–N interaction should be the smaller one, if distance would be the dominant parameter. The interaction of Cd atoms with the other atoms in these MAX phases,

Table 4. Overview of the experimental (RT), extrapolated ($T = 0$ K derived from temperature measurements) and calculated EFGs for ^{111}In/^{111}Cd probes occupying the A- and M-site. The values for V_{zz} are given in units of 10^{21} V m^{-2} and for ν_Q in units of megahertz.

	Experimental (T = RT)		Extrapolated ($T = 0$ K)		DFT calculations A-site		DFT calculations M-site	
Phase	$\lvert V_{zz}\rvert$	ν_Q	$\lvert V_{zz}\rvert$	ν_Q	V_{zz}	ν_Q	V_{zz}	ν_Q
Ti_2InC	15.79(7)	292.0(7)	16.33(4)	302.1(6)	−16.69	308.7	0.39	7.22
Zr_2InC	18.60(7)	344.1(8)	19.75(3)	365.4(4)	−20.17	373.1	1.18	21.80
Ti_2AlN	14.00(9)	258.9(7)	14.36(7)	265.7(1.2)	−13.76	254.5	9.59	177.41
Cr_2GeC	13.49(7)	249.5(8)	13.61(3)	251.7(4)	−14.50	268.2	0.23	4.27

especially when Cd replaces for an M atom, depends also on the nature of the neighboring atoms besides their distance.

5. Summary and conclusions

Selected 211-MAX phases were systematically investigated by PAC experiments with implanted $^{111}\text{In} \rightarrow {}^{111}\text{Cd}$ probes. The challenge of finding the lattice site of the inserted probes was overcome by a systematic comparison of the different compounds. Starting with the key compounds Ti_2InC and Zr_2InC, we observed that the strength of the measured EFGs are of the same magnitude. Due to the close chemical relationship between the A element, In, and the probes used it is evident that this EFG strength is a signature for the A-site. Comparing these results with the quadrupole coupling constants ν_Q found in In-free 211-MAX phases, we conclude, by reason of the similar ν_Q values, that the In probes generally occupy the A-site in these compounds too (cf table 5).

The determination of the M-site EFG will be fixed in the future by a similar series of experiments, using the $^{181}\text{Hf} \rightarrow {}^{181}\text{Ta}$ probe in the key compounds Hf_2InC and Hf_2SnC.

Since the Hf–C bond is much stronger than the Hf–In (Hf–Sn) one, one expects for ion-implanted ^{181}Hf that annealings at higher temperatures and longer durations compared to the ^{111}In implantation have to be applied. In terms of a potential phase decomposition, which might go along with the increased annealings, this issue can be resolved by neutron irradiation of these samples. The natural stable ^{180}Hf transforms due to its high cross section for neutron absorption to ^{181}Hf while the other constituents mostly remain unaffected. By means of this technique the Hf probes already reside the M-site and only moderate annealings have been required to repair the lattice damage.

The population of the X-site by implanted ^{111}In ions can be excluded from geometric and charge considerations (see section 4).

Furthermore, *ab initio* calculations using the APW-lo method, implemented within the WIEN2k code, were performed. They reproduce the experimental EFGs quite well in strength and indirectly confirm that the ^{111}In/^{111}Cd probes were located at the A-site. Had the probes resided on the M-site, the values for the EFG would have been significantly smaller. This is, again, strong evidence that we identified the typical 'A-site EFG' for ^{111}In/^{111}Cd in the 211-MAX phases.

In most cases long annealing steps (several hours) at high temperatures (1000–1300 K) were required to ensure that most of the probes resided at the A-site. Two reasons seem to play an essential role: radiation damage in ceramics and intermetallics anneal at typically 50–75% of the melting points of the compounds. The MAX phases rather decompose into the A element and the corresponding MX carbide/nitride [49, 59, 60] at temperatures usually around 1500–1700 K for MAX phases with heavier A elements like In, Sn and Pb [60] and even higher for lightweight A elements like Al and Si (e.g. approx. 2500 K for Ti_3SiC_2 [60]), it is not surprising that relatively higher annealing temperatures were required herein. However, from the empirical rule of thumb regarding the recovery behavior in the MAX phases, it appears that the annealing temperatures were not directly related to the phase decomposition temperatures. For example, the annealing temperatures for the In-containing phases were found to be in the same range as the temperatures used for the Al-containing phases despite the fact that the decomposition temperatures of the latter are generally higher. Interestingly, the annealing times for the latter compounds were even shorter. This reason may be explained by the fact that the probes did not have to diffuse out of unreacted material agglomerations (i.e. In clusters in Ti_2InC and Zr_2InC) to the A-site. With PAC these clusters could be identified (characteristic EFG for ^{111}In/^{111}Cd in In metal) and it had been shown that after long anneals the fraction of probes in In metal disappeared.

At this moment an important question arises whether we are able to see dissociations of the MAX phases into its A elements and binary carbides or nitrides. As noted above, in most cases no clear evidence for decomposition products during the PAC experiments was found. We observed in Nb_2AsC and Cr_2GeC different probe

Table 5. Summary of PAC parameters measured at room temperatures for different MAX phases after fully annealing. ν_Q is the quadrupole coupling constant describing the strength of the EFG, δ_Q its distribution width, η the asymmetry parameter of the EFG and the fraction shows the maximum percentage of the probes occupying the A-site.

Phase	ν_Q (MHz)	δ_Q (%)	η	Max. frac. (%)
Ti_2InC	292.0(7)	0.8–1.3	0.0	70–90
Zr_2InC (1)	344.1(8)	0.3–0.7	0.0	50–80
Zr_2InC (2)	333.4(1.2)	0.5–1.0	0.0	10–20
Ti_2AlN	258.9(7)	1.0–1.8	0.0	70–90
Nb_2AlC	242.4(6)	1.2–1.5	0.0	70–80
Cr_2GeC	249.6(5)	0.5–0.8	0.0	60–80
Nb_2AsC	323(4)	0.4–1.5	0.0	10–15

surroundings whose signals might be caused by probes located in oxide precipitates (e.g. arsenic oxides) or in complex transition metal phases (e.g. chromium germanium compounds), produced during the anneals and identified afterwards with XRD.

A last complication of this discussion might be the fact that many carbides have a cubic structure, which result in a vanishing EFG (i.e. $\nu_Q = 0$ MHz). But also such a fraction would be detected in the PAC measurement, as the fit gives a fraction with $\nu_Q = 0$ MHz. In this case the perturbation function would be shifted towards higher $-R(t)$ values. This behavior can be seen in the spectra of figure 13. At RT the probes in metallic In precipitates show the known EFG of $\nu_Q = 17.3$ MHz and their fraction is easily fitted. At measuring temperatures T_{meas} above $T_{\text{melt}} = 430$ K In liquefies and then the EFG disappears, i.e. $\nu_Q = 0$ MHz, but the fraction is still observed with the same amount for moderate temperatures below 900 K.

The strange behavior of Zr_2InC is not yet understood. The strong increase of the damping at temperatures between 600 and 900 K may point to a dynamic behavior, where the micro-surrounding is changing. The two EFGs are both very high, but not similar, so that a jump process of the probes or a charge variation in the direct neighborhood can be suspected.

To conclude, this study shows that the isotope ^{111}In is an excellent marker for the A-site in the MAX phases, irrespective of their composition. By knowing the probes' lattice location further statements about the temperature dependence of the EFGs were made. The quadrupole frequencies decreased linearly and reversibly from RT with increasing temperatures. The results of the PAC measurements conform with those from high temperature XRD experiments [44] and link thermal lattice expansions with a decline of the EFGs.

Acknowledgments

The authors gratefully acknowledge the support of D Tallman, B Anasori, M Abdelmalak, M Shamma and J v Lloyd during the MAX phase syntheses, D Purschke for the radioactive ion implantations and V Ebrecht for electronics maintenance. This work was financially supported by the Deutsche Forschungsgemeinschaft (DFG) under contract no. HO 1125/19-1 and by the National Science Foundation (Grant no. DMR 0503711).

References

[1] Catchen G L, Rearick T M and Schlom D G 1994 *Phys. Rev.* B **49** 318
[2] Uhrmacher M and Lieb K P 2000 *Z. Naturf.* a **55** 90
[3] Pleiter F and Hohenemser C 1982 *Phys. Rev.* B **25** 106
[4] Bolse W, Uhrmacher M and Lieb K P 1987 *Phys. Rev.* B **36** 1818
[5] Skudlik H, Deicher M, Keller R, Magerle R, Pfeiffer W, Steiner D, Recknagel E and Wichert T 1992 *Phys. Rev.* B **46** 2159
[6] Ostheimer V, Lany S, Hamann J, Wolf H, Wichert T and Collaboration I 2003 *Phys. Rev.* B **68** 235206
[7] Sato W, Itsuki Y, Morimoto S, Susuki H, Nasu S, Shinohara A and Ohkubo Y 2008 *Phys. Rev.* B **78** 045319
[8] Rearick T M, Catchen G L and Adams J M 1993 *Phys. Rev.* B **48** 224
[9] Bartos A and Uhrmacher M 1993 *Phys. Rev.* B **48** 7478
[10] Damonte L C and Mendoza-Zelis L A 2005 PAC studies on Zr-based intermetallic compounds *HFI/NQI 2004* (Berlin: Springer) pp 317–22 doi:10.1007/3-540-30924-1_51
[11] Cabrera-Pasca G, Saxena R and Carbonari A 2007 *Hyperfine Interact.* **176** 81
[12] Hemmingsen L, Sas K N and Danielsen E 2004 *Chem. Rev.* **104** 4027
[13] Hemmingsen L, Stachura M, Thulstrup P, Christensen N and Johnston K 2010 *Hyperfine Interact.* **197** 255
[14] Barsoum M W 2000 *Prog. Solid State Chem.* **28** 201
[15] Barsoum M W and El-Raghy T 2001 *Am. Sci.* **89** 336
[16] Barsoum M W, Salama I, El-Raghy T, Golczewski J, Seifert H, Aldinger F, Porter W and Wang H 2002 *Metall. Mater. Trans.* A **33** 2775
[17] Lange C, Barsoum M and Schaaf P 2007 *Appl. Surf. Sci.* **254** 1232
[18] Walter C, Sigumonrong D, El-Raghy T and Schneider J 2006 *Thin Solid Films* **515** 389
[19] Eklund P, Beckers M, Jansson U, Högberg H and Hultman L 2010 *Thin Solid Films* **518** 1851
[20] Zhou A, Basu S and Barsoum M 2008 *Acta Mater.* **56** 60
[21] Barsoum M W, Murugaiah A, Kalidindi S R and Zhen T 2004 *Phys. Rev. Lett.* **92** 255508
[22] Schatz G and Weidinger A 1995 *Nuclear Condensed Matter Physics* (New York: Wiley) pp 88–9
[23] Arends A R, Hohenemser C, Pleiter F, de Waard H, Chow L and Suter R M 1980 *Hyperfine Interact.* **8** 191
[24] Raman S and Kim H 1971 *Nucl. Data Sheets* **6** 39
[25] Ellis Y A 1973 *Nuclear Data Sheets* **9** 319
[26] Wegner D 1985 *Hyperfine Interact.* **23** 179
[27] Attili R N, Uhrmacher M, Lieb K P, Ziegeler L, Mekata M and Schwarzmann E 1996 *Phys. Rev.* B **53** 600
[28] Attili R N, Saxena R N, Carbonari A W, Mestnik Filho J, Uhrmacher M and Lieb K P 1998 *Phys. Rev.* B **58** 2563
[29] Jürgens D, Uhrmacher M, Hofsäss H, Röder J, Wodniecki P, Kulinska A and Barsoum M W 2007 *Hyperfine Interact.* **178** 23
[30] Schwarz K and Blaha P 2003 *Comput. Mater. Sci.* **28** 259
[31] Schwarz K 2003 *J. Solid State Chem.* **176** 319
[32] Uhrmacher M, Neubauer M, Bolse W, Ziegeler L and Lieb K P 1998 *Nucl. Instrum. Methods* B **139** 306
[33] Uhrmacher M, Pampus K, Bergmeister F, Purschke D and Lieb K 1985 *Nucl. Instrum. Methods* B **9** 234
[34] Haas H and Correia J 2010 *Hyperfine Interact.* **198** 133 doi:10.1007/s10751-010-0211-6
[35] Nagl M, Vetter U, Uhrmacher M and Hofsäss H 2010 *Rev. Sci. Inst.* **81** 073501
[36] Nagl M 2011 Pac-suite project page http://pac-suite.sf.net
[37] Butz T 2011 private communications
[38] Haas H and Shirley D A 1973 *J. Chem. Phys.* **58** 3339
[39] Barsoum M W, Golczewski J, Seifert H J and Aldinger F 2002 *J. Alloys Compounds* **340** 173
[40] Jürgens D, Uhrmacher M, Hofsäss H, Mestnik-Filho J and Barsoum M W 2010 *Nucl. Instrum. Methods* B **268** 2185
[41] Vianden R 1983 *Hyperfine Interact.* **16** 1081
[42] Salama I, El-Raghy T and Barsoum M W 2002 *J. Alloys Compounds* **347** 271
[43] Company S-W S 1971 *Periodic Table of the Elements* (Skokie, IL: Sargent-Welch Scientific Co.)
[44] Scabarozi T H *et al* 2009 *J. Appl. Phys.* **105** 013543
[45] Christiansen J, Heubes P, Keitel R, Klinger W, Loeffler W, Sandner W and Witthuhn W 1976 *Z. Phys.* B **24** 177
[46] Wodniecki P, Wodniecka B, Kulinska A, Uhrmacher M and Lieb K P 2004 *J. Alloys Compounds* **385** 53

[47] Wodniecki P, Wodniecka B, Kulinska A, Uhrmacher M and Lieb K P 2002 *J. Alloys Compounds* **335** 20
[48] Kulinska A, Wodniecki P, Wodniecka B, Petrilli H M, Terrazos L A, Uhrmacher M and Lieb K P 2009 *J. Phys.: Condens. Matter* **21** 095405
[49] Ganguly A, Barsoum M W and Doherty R D 2007 *J. Am. Ceram. Soc.* **90** 2200
[50] Wiarda D, Uhrmacher M, Bartos A and Lieb K P 1993 *J. Phys.: Condens. Matter* **5** 4111
[51] Hohenberg P and Kohn W 1964 *Phys. Rev.* **136** B864
[52] Kohn W and Sham L J 1965 *Phys. Rev.* **140** A1133
[53] Cottenier S 2002 *Density Functional Theory and the Family of (L)APW-Methods: A Step-by-Step Introduction* (K U Leuven: Instituut voor Kern- en Stralingsfysica)
[54] Madsen G K H, Blaha P, Schwarz K, Sjöstedt E and Nordström L 2001 *Phys. Rev.* B **64** 195134
[55] Blaha P, Schwarz K, Madsen G, Kvasnicka D and Luitz J 2009 *WIEN2k, An Augmented Plane Wave Plus Local Orbitals Program for Calculating Crystal Properties* (Wien: Technische Universität Wien) http://www.wien2k.at/reg_user/textbooks/userguide.pdf
[56] Perdew J P, Burke K and Ernzerhof M 1996 *Phys. Rev. Lett.* **77** 3865
[57] He X, Bai Y, Li Y, Zhu C and Li M 2009 *Solid State Commun.* **149** 564
[58] Medkour Y, Bouhemadou A and Roumili A 2008 *Solid State Commun.* **148** 459
[59] Barsoum M W, Yaroschuk G and Tyagi S 1997 *Scr. Mater.* **37** 1583
[60] El-Raghy T, Chakraborty S and Barsoum M W 2000 *J. Eur. Ceram. Soc.* **20** 2619
[61] Ganguly A, Barsoum M W and Schuster J 2005 *J. Am. Ceram. Soc.* **88**
[62] Hoffman E, Barsoum M W, Wang W, Doherty R D and Zavaliangos A 2005 On the spontaneous growth of soft metallic whiskers *Proc. 51st IEEE Holm Conf. on Electrical Contacts (26–28 Sept. 2005)* pp 121–6 doi:10.1109/HOLM.2005.1518232
[63] Drulis M K, Drulis H, Hackemer A, Ganguly A, El-Raghy T and Barsoum M 2007 *J. Alloys Compounds* **433** 59
[64] Amini S, Zhou A, Gupta S, Devillier A, Finkel P and Barsoum M W 2008 *J. Mater. Res.* **23** 2157
[65] Kumar R S, Rekhi S, Cornelius A L and Barsoum M W 2005 *Appl. Phys. Lett.* **86** 111904
[66] Jeitschko F B W and Nowotny H 1963 *Monatsh. Chem.* **94** 1201